8-1-2021

Distribution of Glutamatergic and Glycinergic Inputs onto Human Auditory Coincidence Detector Neurons.

Yusra Mansour
Henry Ford Health, ymansou1@hfhs.org

Randy Kulesza

Recommended Citation

Mansour Y, and Kulesza R. Distribution of Glutamatergic and Glycinergic Inputs onto Human Auditory Coincidence Detector Neurons. Neuroscience 2021; 468:75-87.

NEUROSCIENCE
RESEARCH ARTICLE
Y. Mansour, R. Kulesza / Neuroscience 468 (2021) 75–87

Distribution of Glutamatergic and Glycinergic Inputs onto Human Auditory Coincidence Detector Neurons

Yusra Mansour [a,b] **and Randy Kulesza** [a]*

[a] *Department of Anatomy, Lake Erie College of Osteopathic Medicine, Erie, PA, United States*

[b] *Henry Ford Macomb Hospital, Department of Otolaryngology – Facial Plastic Surgery, Clinton Township, MI, United States*

Abstract—Localization of sound sources in the environment requires neurons that extract interaural timing differences (ITD) in low-frequency hearing animals from fast and precisely timed converging inputs from both ears. In mammals, this is accomplished by neurons in the medial superior olive (MSO). MSO neurons receive converging excitatory input from both the ipsilateral and contralateral cochlear nuclei and glycinergic, inhibitory input by way of interneurons in the medial and lateral nuclei of the trapezoid body (MNTB and LNTB, respectively). Key features of the ITD circuit are MSO neurons with symmetric dendrites that segregate inputs from the ipsilateral and contralateral ears and preferential distribution of glycinergic inputs on MSO cell bodies. This circuit for ITD is well characterized in gerbils, a mammal with a prominent MSO and a low-frequency hearing range similar to humans. However, the organization of this circuit in the human MSO has not been characterized. This is further complicated by limited understanding of the human LNTB. Nonetheless, we hypothesized that the ITD circuit characterized in laboratory animals is similarly arranged in the human MSO. Herein, we utilized neuron reconstructions and immunohistochemistry to investigate the distribution of glutamatergic and glycinergic inputs onto human MSO neurons. Our results indicate that human MSO neurons have simple, symmetric dendrites and that glycinergic inputs outnumber glutamatergic inputs on MSO cell bodies and proximal dendrites. Together these results suggest that the human MSO utilizes similar circuitry to other mammals with excellent low-frequency hearing.

Key words: hearing, auditory, brainstem.

INTRODUCTION

The mammalian auditory system functions to characterize the origin as well as temporal and spectral features of a large repertoire of environmental sounds and vocalizations. Mechanoreceptors in the organ of Corti and the central auditory pathways are organized according to maps of sound frequency, or tonotopy, and these maps are evident in most if not all auditory nuclei and tracts (Guinan et al., 1972). However, localization of sound sources in the environment requires extraction of information beyond frequency. Specifically, circuits that function in localization of low-frequency sounds compare the arrival time of sounds at each ear and calculate an interaural time difference (ITD; Jeffress, 1948; Goldberg and Brown, 1969; Yin and Chan, 1990; Spitzer and Semple, 1995). This task requires circuits specialized for fast and precise convergence of information from both ears (Grothe et al., 2010). In the mammalian auditory brainstem, neurons in the medial superior olive (MSO) are the first major site of convergence of information from both ears and these neurons play an essential role in extracting ITDs (Stotler, 1953; Goldberg and Brown, 1969; Yin and Chan, 1990; Brand et al., 2002; Couchman et al., 2010). Specifically, ITD coding depends on maximal responses to coincidental excitatory inputs from each ear and consistent with this function, MSO neurons are referred to as coincidence detectors (Kapfer et al., 2002). Indeed, MSO neurons are capable of detect-

*Corresponding author at: Department of Anatomy, Lake Erie College of Osteopathic Medicine, 1858 West Grandview Blvd, Erie, PA 16504, United States.
E-mail address: rkulesza@lecom.edu (R. Kulesza).

Abbreviations: AN, auditory nerve; CB, calbindin; CI, confidence interval; CR, calretinin; ctt, central tegmental tract; FN, facial nucleus; GABA, gamma aminobutyric acid; GBC, globular bushy cells; GlyR, glycine receptor; ITD, interaural time difference; L, lateral; ll, lateral lemniscus; LNTB, lateral nucleus of the trapezoid body; LSO, lateral superior olive; M, medial; MAP2, microtubule associated protein; ml, medial lemniscus; MNTB, medial nucleus of the trapezoid body; MSO, medial superior olive; NHS, normal horse serum; NTR, neurotrace red; P, posterior; PB, phosphate buffer; PBS, phosphate buffered saline; PN, pontine nuclei; PVCN, posterior ventral cochlear nucleus; pvLNTB, posteroventral lateral nucleus of the trapezoid body; R, rostral; SBC, spherical bushy cells; SD, standard deviation; SOC, superior olivary complex; SPON, superior paraolivary nucleus; STN, spinal trigeminal nucleus; stt, spinal trigeminal tract; tz, trapezoid body; VCN, ventral cochlear nucleus; VGLUT, vesicular glutamate transporter 1; VI, abducens nerve; VIAAT, vesicular inhibitory amino acid transporter; VII, facial nerve; VNTB, ventral nucleus of the trapezoid body.

https://doi.org/10.1016/j.neuroscience.2021.06.004
0306-4522/

ing ITDs in the microsecond range and such precision is required to accurately localize sound sources in the environment (Klumpp and Eady, 1956; Goldberg and Brown, 1969; Yin and Chan, 1990; Brand et al., 2002; Grothe et al., 2010; van der Heijden et al., 2013).

In nearly all mammalian species, the MSO consists of a stacked column of elongated neurons that give rise to both medially and laterally directed dendrites (Stotler, 1953; Feng and Rogowski, 1980; Kiss and Majorossy, 1983). While there is abundant input onto the cell body of MSO neurons, this dendritic organization serves to collect and segregate inputs from the ipsilateral and contralateral ears (Stotler, 1953; Grothe et al., 2010). Inputs to the MSO are comparatively simple and well characterized in several laboratory animals (Brand et al., 2002, Pecka et al., 2008; Couchman et al., 2012; van der Heijden et al., 2013; Myoga et al., 2014; Fig. 1). The MSO receives glutamatergic input from both ears via spherical bushy cells (SBCs) in the ventral cochlear nuclei (VCN). Inhibitory input from the ipsilateral ear is driven by glutamatergic input from globular bushy cells (GBC) to the lateral nucleus of the trapezoid body (LNTB) and inhibitory input from the contralateral ear is driven by GBC input to the medial nucleus of the trapezoid body (MNTB; Friauf and Ostwald, 1988; Kuwabara et al., 1991; Smith et al., 1991). Together, the LNTB and MNTB provide monoaural glycinergic input from each ear to the MSO (Kuwabara and Zook, 1992; Grothe and Sanes, 1993; Smith, 1995; Smith et al., 1998; Roberts et al., 2014). Despite the added synaptic delay for MNTB and LNTB inputs to the MSO, these glycinergic inputs reach the MSO before the glutamatergic inputs from SBCs (Roberts et al., 2014). The speed and precision required for this circuit is mediated by several specializations. Specifically, GBCs give rise to large diameter, heavily myelinated axons and form large calyx terminals upon MNTB/LNTB somata that include hundreds of synapses/active zones (Morest, 1968a, 1968b; Banks and Smith, 1992; Cant and Hyson, 1992; Spirou and Berrebi, 1996, 1997; Taschenberger et al., 2002). Furthermore, GBC axon diameter, myelination and inter-nodal lengths vary across best-frequency and are optimized for ITD coding (Ford et al., 2015). These glycinergic inputs from the MNTB/LNTB are preferentially distributed onto the soma of MSO neurons in laboratory animals with excellent low-frequency hearing and that preferentially use ITDs (Clark, 1969 [cat]; Kapfer et al., 2002; Couchman et al., 2010 [gerbil]). Accordingly, these glycinergic inputs to the MSO play an essential role in fine tuning ITDs (Brand et al., 2002; Grothe and Sanes, 1993; van der Heijden et al., 2013; Myoga et al., 2014).

While the ITD circuit is well characterized in animal models, virtually nothing is known about the ITD circuit in the human MSO. The MSO is the largest and most prominent nuclei of the human superior olivary complex (SOC), and this is consistent with excellent low-frequency hearing in humans (Kulesza, 2007). The human MSO includes about 15,000 fusiform or triangular cell bodies that emit both medial and lateral primary dendrites perpendicular to the long axis of the nucleus. While the human ITD circuits are likely consistent with pathways that have been demonstrated in gerbils, the contributions of the MNTB and LNTB are unclear. This is further complicated by a decades long debate about the human MNTB in humans (Moore and Moore, 1971; Strominger and Hurwitz, 1976; Moore, 1987; Bazwinsky et al., 2003; Hilbig et al., 2009; but see Kulesza, 2014; Kulesza and Grothe, 2015) and a number of uncertainties regarding the structure and connectivity of the LNTB. Regardless, we hypothesized that inhibitory and excitatory inputs are segregated onto human MSO neurons. Specifically, that inhibitory, glycinergic inputs are preferentially distributed on the soma and proximal dendrites while excitatory, glutamatergic inputs are preferentially distributed on more distal dendrites. We chose to examine this hypothesis by first characterizing the dendritic architecture of human MSO neurons using silver impregnation and immunohistochemistry. We then utilized immunohistochemistry to quantify the distribution of the calcium binding protein calretinin (CR) as a marker for inputs from SBCs, and vesicular glutamate transporter 1 (VGLUT) for excitatory inputs from the VCN (Ito et al., 2015), and we identified inhibitory inputs using antibodies for the vesicular inhibitory amino acid transporter (VIAAT), the GABA/glycine anchor protein gephyrin and the glycine receptor (GlyR).

EXPERIMENTAL PROCEDURES

Materials and fixation

This investigation is based on the study of 14 human brainstems from individuals ranging in age from 57 to 93 years of age (mean 79 ± 10 years of age; 7 males and 7 females). Table 1 shows age, cause of death and post-mortem interval for the subjects in this study. Subjects were donated to the Lake Erie College of Osteopathic Medicine through the Pennsylvania Humanity Gifts Registry; brain removal was deemed exempt by the xxx Institutional Review Board. Brainstem specimens were used in this study if: the cause of death was not neurological, there were no external or internal signs of neurodegenerative disease, there were no signs of pathology impacting the brainstem or posterior cranial fossa (e.g. meningioma, hemorrhage) and brainstems could be preserved within 24 h of death. Specimens 06.19 through 09.45 were perfused through the right common carotid artery with embalming solution (33.3% glycerin, 33.3% methanol, 27.8% phenol and 5.6% formaldehyde, diluted 1:3 in water; King Chemical, Inc., St. Louis, Missouri) and dissected from the skull after a short post-embalming interval. The remaining specimens were dissected from the skull immediately upon arrival to the morgue. These specimens were trimmed to tissue blocks including the SOC, post-fixed for at least 2 weeks in 4% paraformaldehyde in 0.1 M phosphate buffer (PB), pH 7.2. Consistent with our previous work in the human auditory brainstem and radiological convention, we use the directional terms anterior (ventral in rodents) and posterior (dorsal in rodents; Kulesza, 2008).

Four brainstems were processed for silver impregnation (Friedland et al., 2006; Kulesza, 2007: table

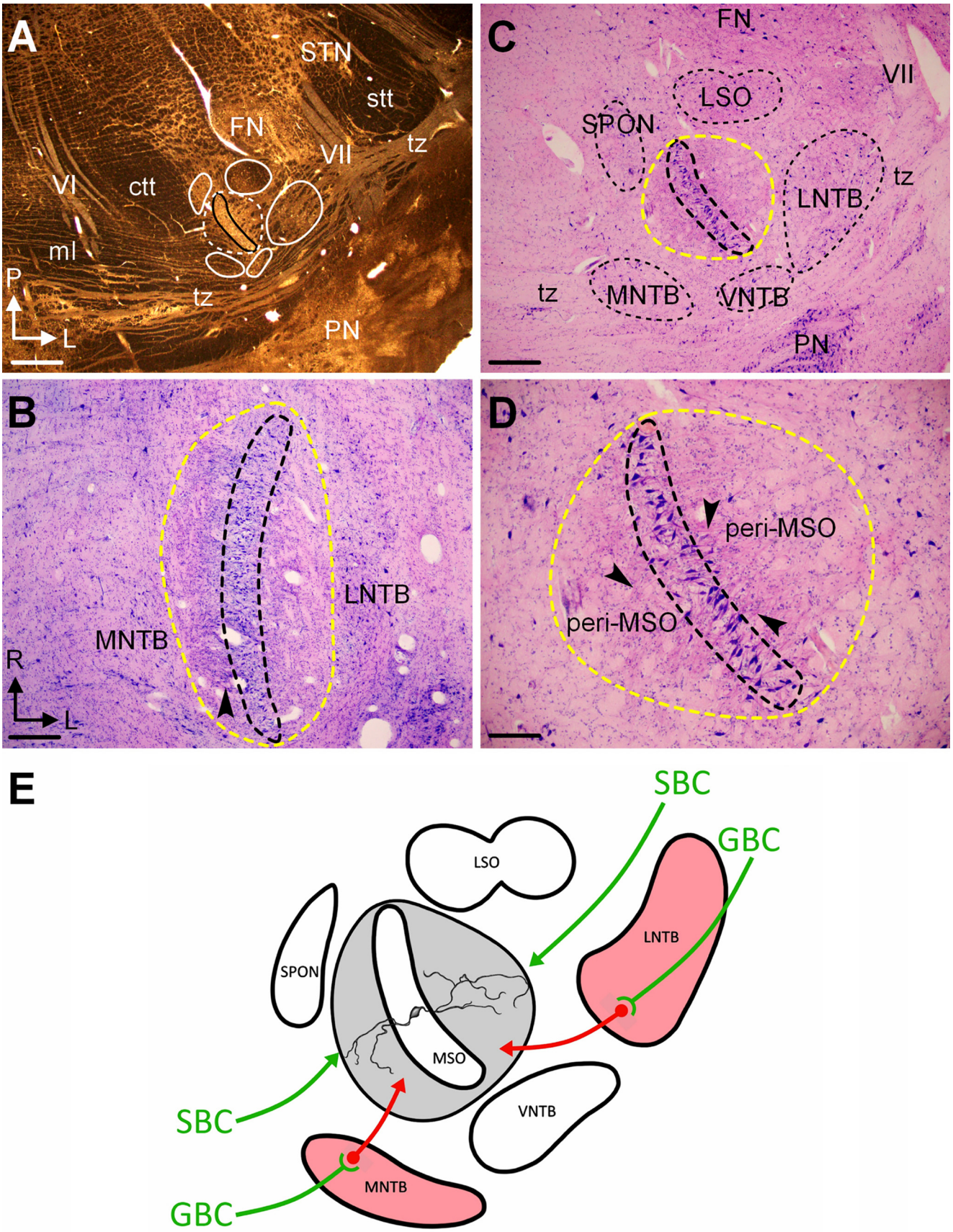

Table 1. Subjects.

Brain No.	Age	Sex	Cause of death	PMI (hrs)	Techniques
06.19	89	M	cardiac	< 24	Golgi
06.20	93	M	cardiac	< 24	Golgi
06.21	84	F	myocardial infarction	< 24	Golgi
07.02	77	M	cardiac	< 24	Golgi
09.45	72	F	arrhythmia	< 24	IHC
10.01	57	M	respiratory failure	< 24	IHC
11.62	83	F	atrial fibrillation	18	IHC
11.63	84	F	breast cancer	< 5	IHC
11.64	77	F	diabetes, renal	8	IHC
13.05	79	M	COPD	7	IHC
16.16	91	M	renal failure	8	IHC
18.01	73	M	renal failure	4	IHC
18.45	62	F	pancreatic cancer	6	IHC
20.02	85	F	failure to thrive	10	IHC

1) and used to reconstruct MSO neurons. Tissue blocks including the SOC were incubated in fixative (at 4 °C) for at least 30 days and cut into 3–5 mm thick blocks (in the transverse plane). These blocks were incubated in a solution of 5% chloral hydrate, 5% potassium dichromate and 10% formaldehyde in distilled water, in the dark, for four days under a continuous vacuum of 68 kPa. Tissue blocks were rinsed in 1% silver nitrate in distilled water, brushed clear of debris and incubated in 1% silver nitrate for four days under continuous vacuum in the dark. Tissue blocks were then sectioned on a vibratome at a thickness of 200 μm, mounted onto glass slides, dried and cover slipped. Impregnated neuron profiles were reconstructed with the aid of an Olympus BX45 microscope and a drawing tube attachment. These tracings were digitized, and dendritic profiles were quantified using ImageJ (version 1.52p; Schneider et al., 2012). Dendrite length (cell body to distal tip) and anterior-posterior spread was measured in 12 medial dendrites and 11 lateral dendrites. Dendritic complexity of 14 MSO neurons was quantified using the Sholl Analysis feature. Briefly, dendritic intersections were counted on concentric hemishells (left and right) at intervals of 50 μm extending up to 300 μm from the parent soma.

Immunohistochemistry and immunofluorescence

Tissue blocks used for immunohistochemistry were cryoprotected in 30% sucrose and 4% paraformaldehyde in 0.1 M PB until they were saturated (approximately 2 weeks), sectioned in the transverse or coronal plane on a freezing microtome and collected in 0.1 M PB. Alternating series of sections were designated for cell body staining (Giemsa; Iñiguez et al., 1985) or myeloarchitecture (Aparicio and Saldaña, 2014; Márquez-Legorreta et al., 2016).

The distribution of the vesicular glutamate transporter (VGLUT), calretinin (CR), microtubule associated protein-2 (MAP2) and the potassium channel Kv3.1b were examined using chromogenic labelling. Briefly, tissue sections were rinsed in 0.1 M PB, endogenous peroxidase activity was quenched in a wash of 1.5% hydrogen peroxide in PB. Tissue sections were permeabilized in 0.5% Triton X, blocked in 1% normal donkey serum (NDS) for 1 h and incubated overnight with primary antisera diluted in 1% NDS in PB at room temperature. The antisera and dilutions used in this investigation are summarized in Table 2. Sections were then rinsed, incubated for 1–2 h in biotinylated secondary antisera (Vector Laboratories, Burlingame, California; 1:100 in PB) then incubated in a solution of avidin–biotin complex for 1–2 h (Vector Laboratories, Elite Kit). Sections were thoroughly rinsed, and the chromogen reaction was developed in 0.05% diaminobenzidine and 0.01% hydrogen peroxide with heavy metal intensification (nickel ammonium sulfate; Adams, 1981). Finally, sections were mounted onto glass slides from gelatin alcohol and selected sections were counterstained with Neutral Red and sealed under coverslips with Permount (Fisher Scientific, Pittsburgh, PA, USA).

The distribution of the vesicular inhibitory amino acid transporter (VIAAT), glycine receptor (GlyR), the glycine receptor linker protein gephyrin and the neurofilament

Fig. 1. The human MSO. Shown in **(A)** is a fresh section through the caudal pons demonstrating myeloarchitecture of the SOC (transverse section). The human MSO (black outline) is evident as a thin curvilinear column surrounded by the peri-MSO field (white dashed line) and SOC nuclei. Shown in **(B)** is a Giemsa-stained coronal section through the SOC showing the rostro-caudal extent of the MSO (black dashed line) and the peri-MSO (yellow dashed line). The arrowheads indicate bundles of dendrites extending from the MSO cell column into the peri-MSO. Shown in **(C)** and **(D)** are Giemsa-stained transverse sections through the SOC illustrating the peri-MSO (yellow dashed line). Figure **(D)** illustrates the morphology of human MSO neurons and bundles of dendrites extending into the peri-MSO. Figure **(E)** Summarizes the general pattern of inputs to the mammalian MSO on a schematic of the human SOC. The MSO receives glutamatergic inputs (green) from SBCs in both the ipsilateral and contralateral cochlear nuclei and glycinergic inputs (red) from each ear by way of the MNTB and LNTB. The scale bars are as follows: A = 1 mm, B, C = 500 μm, D = 200 μm. Abbreviations: R – rostral, L – lateral, P – posterior.

Table 2. Antibodies and dilutions

Target	Species	Dilution	Sources	Method
Calretinin	rabbit	1:100	Abcam	DAB
Kv3.1b	mouse	1:1000	NeuroMab	DAB
MAP2	mouse	1:1000	EMD Millipore	DAB
VGLUT1	rabbit	1:1000	Sigma-Aldrich	DAB
Gephyrin	rabbit	1:1000	EMD Millipore	IF
Glycine R (α1/α2)	rabbit	1:1000	Abcam	IF
SMI-311	mouse	1:1000	Abcam	IF
VIAAT	rabbit	1:1000	Sigma-Aldrich	IF

SMI-311 were examined using immunofluorescence. Free-floating tissue sections were rinsed in 0.1 M phosphate buffered saline (PBS) and blocked for 1 h in 1% normal horse serum (NHS) and 0.5% triton-X. Sections were incubated overnight in primary antisera (Table 2) with 1% NHS in PBS, rinsed, incubated for 2 h in goat anti-rabbit DyLight 488 (Vector Labs, Burlingame, CA, USA), counterstained with Neurotrace Red (NTR; a fluorescent Nissl stain) and rinsed. Lipofuschin autofluorescence was quenched by a 5 min incubation in 0.1% Sudan Black. Sections were rinsed in 70% ethanol, mounted and coverslipped with PB. Photomicrographs were taken with a DP71 digital camera on an Olympus CKX41 microscope or a Leica TCS SP5 confocal microscope.

Quantification

Peri-somatic puncta were counted around identified cell bodies and are presented as VGLUT/CR/VIAAT-positive (+) puncta per cell body area (puncta/μm^2). We did not include proximal dendrites in our counts of peri-somatic puncta. Peri-dendritic puncta were counted along proximal dendrite segments emerging from MSO soma and are presented as puncta/100 μm. Puncta in the peri-MSO fields were counted using a 200 $\times$ 200 μm grid that formed 40,000 μm^2 (0.04 mm^2) boxes. These counting boxes were situated within both the medial and lateral peri-MSO fields. Counting boxes up to 270 μm from the MSO cell column were considered near (medial and lateral) and boxes beyond 400 μm from the MSO cell column were considered far (medial and lateral). Table 3 provides a summary of the number of neurons and puncta counted for this study.

Statistics

Descriptive statistics were generated for all data sets using GraphPad Prism 8.4.3 (GraphPad Software, La Jolla, CA, USA). All data sets were tested against a normal distribution using the D'Agostino & Pearson omnibus normality test. If a data set fits the normal distribution, comparisons were conducted using parametric tests (i.e., *t* test) and results are presented as mean ± standard deviation. If a data set failed to fit the normal distribution, comparisons were conducted using nonparametric tests and are presented as the median with the 95% confidence interval (CI) of the median. Regardless of normality, data are presented in the figures with box and whiskers plots depicting the 25th and 75th quartiles and whiskers show the 5th and 95th percentiles, respectively. Data points beyond these percentiles are shown in the graphs as symbols. Data from the Sholl analysis were modeled as straight lines and examined using simple linear regression. A 2-way ANOVA was conducted to examine any differences between transporters (VGLUT, VIAAT) and location within the peri-MSO. These data are shown in Fig. 6 and all data points are provided. Differences were considered statistically significant if p values were < 0.05.

RESULTS

Dendrites of human MSO neurons

In the human brainstem, the MSO forms a curvilinear column of densely packed somata. In fresh (unstained) tissue sections, the MSO cell column is evident as a pale area within the SOC, anteromedial to the facial nucleus (FN) and posterior to the transversely running axons of the trapezoid body (tz; Fig. 1A). Human MSO neurons are fusiform or triangular in shape and arranged in a thin column, 3–5 neurons wide, evident in coronal (Fig. 1B) and transverse sections (Fig. 1C, D). Both medial and lateral to the MSO cell column is a peri-MSO field that is generally devoid of neuronal cell bodies, but rich in glia, dendrites and myelinated axons (Fig. 1A, D). The peri-MSO field is evident along the

Table 3. Summary of puncta counts

	VGAT+	Gephyrin+	VGLUT+	CR+
Cell bodies	1235 (214 cells)	900 (54 cells)	350 (146 cells)	143 (69 cells)
Proximal dendrites	1325 (156 dendrites)	120 (78 dendrites)	127 (60 dendrites)	143 (40 dendrites)
Peri-MSO	988 (32 fields)		1331 (35 fields)	

entire rostro-caudal aspect of the nucleus (Fig. 1B). In Giemsa-stained sections, dendrites of MSO neurons are evident as slender eosinophilic profiles emerging from cell bodies and extending into the peri-MSO fields (Fig. 1B, D, black arrowheads). We sought to further characterize dendrites of human MSO neurons using immunohistochemistry and silver staining.

Kv3.1b immunolabelling was present in nearly all human MSO neurons (Fig. 2A). Kv3.1b labelling extended into dendrites that could be traced over 400 μm into the peri-MSO (Fig. 2A, black arrowheads). Similarly, MAP2 immunolabeling was present in nearly all MSO cell bodies and dendrites (Fig. 2B). Bundles of MAP2+ dendrites extended from the MSO cell column into the peri-MSO. Together, Kv3.1b and MAP2 immunolabelling confirm dendrites of MSO neurons extend into the peri-MSO fields and occupy a significant portion of this compartment (Fig. 2A, B, arrowheads). We then examined symmetry and complexity of human MSO neurons by reconstructing neurons from silver impregnated tissue. Each MSO neuron gave rise to a medial and lateral dendrite and these emerged perpendicular to the long axis of the parent MSO neuron and extended into the peri-MSO field (Fig. 2C). Medial dendrites (n = 12) extended 125 ± 67 μm (mean ± SD) from the soma and had a maximum anterior-posterior divergence of 121 ± 52 μm (Fig. 2D, E). Lateral dendrites (n = 11) extended 151 ± 66 μm from the soma and had a maximum anterior-posterior divergence of 115 ± 75 μm (Fig. 2D, E). There was no difference in dendrite length ($t(21)$ = 0.94, p = 0.35) or anterior-posterior (AP) divergence ($t(21)$ = 0.19, p = 0.84) between medial and lateral dendrites.

Each primary dendrite typically give rise to 1–2 secondary branches directed into the medial peri-MSO field and 1–2 secondary branches directed to the lateral field (Fig. 2C–F). Overall, lateral dendrites form relatively few branches as they extend into the peri-MSO (Fig. 2C). However, there was more extensive branching from medial dendrites and this difference was more evident on dendrites more than 150 μm from the parent soma (n = 14 neurons; Fig. 2C–F; F = 5.874, DFn = 1, DFd = 8, p = 0.04).

Inputs onto MSO cell bodies and proximal dendrites

Cell bodies of human MSO neurons are contacted by VGLUT, CR and VIAAT+ puncta, however the density of these puncta varies (Fig. 3). Specifically, cell bodies in the MSO were associated with 0.5 (CI: 0.17–0.42) VGLUT+ puncta per 100 μm^2 and 0.6 (CI: 0.32–0.69) CR+ puncta per 100 μm^2 (Fig. 3A, B; arrowheads). There was no difference between the number of VGLUT and CR+ puncta. However, there were many more VIAAT+ puncta (2.1 [CI: 1.9–2.3] per 100 μm^2; Fig. 3C-E, arrowheads) and there were more VIAAT+ puncta on MSO cell bodies compared to VGLUT and CR+ puncta (Fig. 3F; 7).

On MSO proximal dendrites (emerging from cell bodies) there were 1.7 (CI: 1.1–2.9) VGLUT+ puncta per 100 μm and 1.8 (CI: 1–2.7) CR+ puncta per 100 μm (Fig. 3A, B; arrows). There was no difference between the number of VGLUT and CR+ puncta. However, there were 11 (CI: 8.8–11.7) VIAAT+ puncta per 100 μm (Fig. 3C–E; white arrow).

Given the high density of VIAAT+ terminals in the MSO, we sought to correlate this with localization of the glycine receptor (GlyR) and the GlyR anchor protein, gephyrin. Immunolabelling for the GlyR revealed abundant labelling along the MSO cell column and this extended into the peri-MSO fields (Fig. 4A). GlyR immunolabelling was evident along cell bodies (Fig. 4B, arrowheads) and dendrites (Fig. 4B, arrows). Further, confocal imaging for gephyrin revealed a high density of gephyrin+ puncta along MSO cell bodies and SMI-311+ dendrites (Fig. 5). Gephyrin+ puncta are shown in Fig. 5C–E. Specifically, MSO cell bodies were associated with 31.8 (CI: 28–38) gephyrin+ puncta per 100 μm^2 (Fig. 5A–C; white arrowheads) and proximal MSO dendrites were associated with 4.3 (CI: 0–24) gephyrin+ puncta per 100 μm on MSO proximal dendrites (Fig. 5A–C, D; cyan arrowheads).

Inputs to the peri-MSO field

Since human MSO cell bodies and primary dendrites appear to have disproportionate distributions of VIAAT and VGLUT puncta, we sought to examine these inputs on distal dendrites within the peri-MSO. In both the medial and lateral peri-MSO fields there are numerous VGLUT and VIAAT+ puncta (Fig. 6). In the medial peri-MSO field there were 35 (CI: 25–51) VGLUT+ puncta/0.04 mm^2 near (M1) and 34 (CI: 33–45) far (M2) from the MSO cell column (Fig. 6A). In the lateral peri-MSO field there were 35 (CI: 33–43) VGLUT+ puncta/0.04 mm^2 near (L1) and 41 (CI: 35–45) puncta far (L2) from the MSO cell column (Fig. 6A). There was no difference in the density of VGLUT+ puncta across the peri-MSO field ($H(4)$ = 3.2, p = 0.36; Fig. 6C; 7).

In the medial peri-MSO field there were 35 (CI: 15–44) VIAAT+ puncta/0.04 mm^2 near (<270 μm; M1) and 34 (CI: 14–38) far (>400 μm; M2) from the MSO cell column (Fig. 6B). In the lateral peri-MSO field there were 32 (CI: 21–65) VIAAT+ puncta near (L1) and 26 (CI: 16–38) far (L2) from the MSO cell column (Fig. 6B). There was no difference in the density of VIAAT+ puncta across the peri-MSO field ($H(4)$ = 0.41, p = 0.93; Fig. 6C). A 2-way ANOVA comparing the density of VGLUT and VIAAT+ puncta over different regions of the peri-MSO fields revealed a significant effect of transporter ($F(1,59)$ = 7.5, p = 0.008; Fig. 6C). Specifically, there was a significantly higher density of VGLUT+ puncta in the far lateral field (L2) compared to VIAAT (p = 0.02; Fig. 6C; 7)

DISCUSSION

This report provides the first quantitative analysis of dendritic architecture of human MSO neurons and the first analysis of the distribution of VGLUT, VIAAT, GlyR and gephyrin in the human MSO. We show that human MSO cell bodies emit dendrites into both sides of the peri-MSO, and that these dendrites are nearly

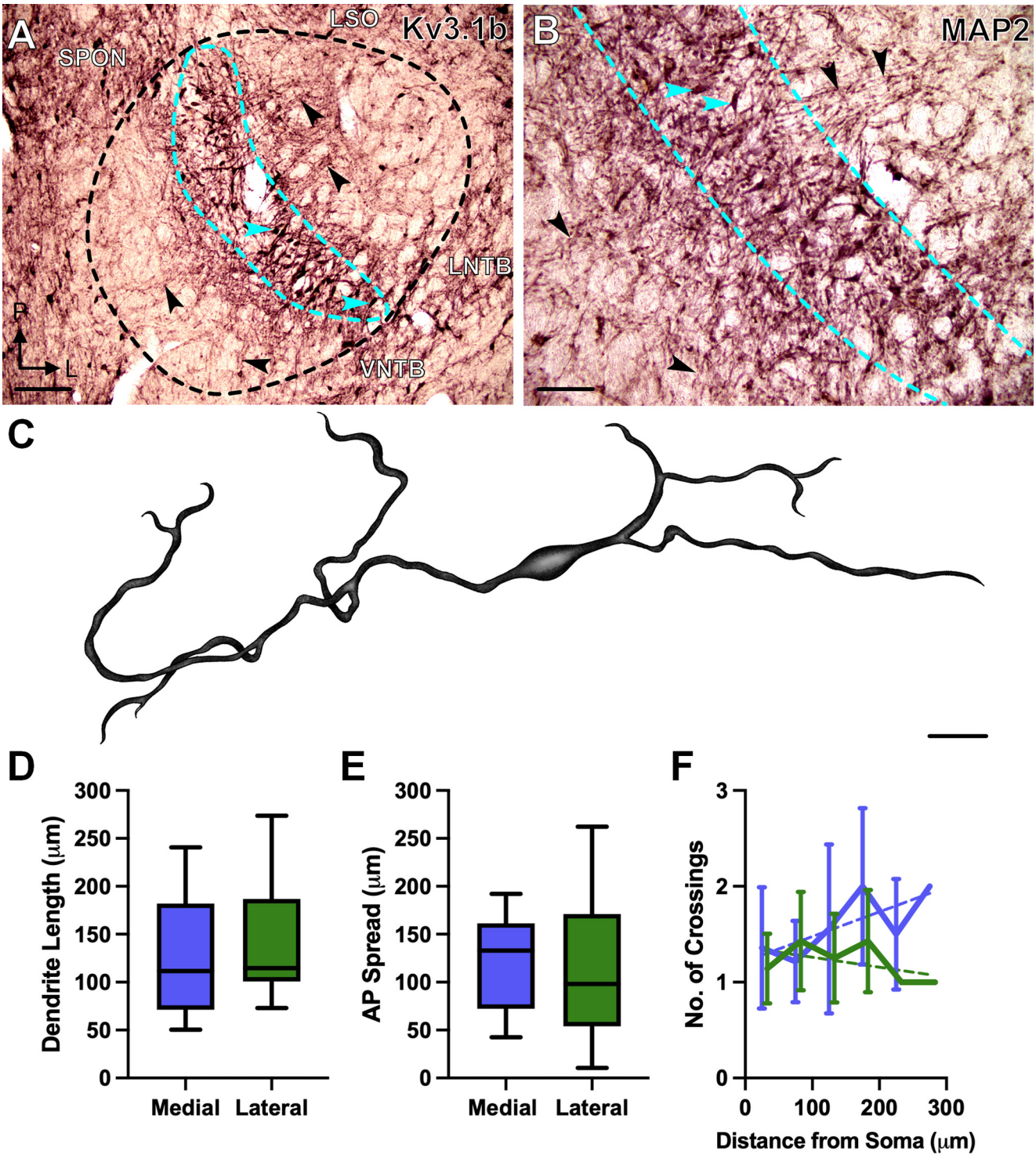

Fig. 2. Features of human MSO dendrites. Shown in **(A)** is immunolabeling for Kv3.1b in the MSO. The MSO cell column is indicated by the cyan dashed line and the peri-MSO by the black dashed line. Kv3.1b labeling is found in somata (cyan arrowheads) and dense bundles of dendrites (black arrowheads) extending into the peri-MSO. Immunolabeling for the cytoskeletal marker MAP2 reveals a similar pattern in the MSO, with MAP2 labeling in cell bodies (cyan arrowheads) and bundles of dendrites (black arrowheads). Shown in **(C)** is a reconstructed human MSO neuron from silver impregnated sections (same orientation as **(A)** and **(B)**). Shown in **(D)** and **(E)** are lengths and spread (divergence) of reconstructed MSO dendrites from the medial and lateral peri-MSO. Shown in **(F)** are plots of the number of dendritic branches over their distance from the parent soma (solid lines) and simple linear regression (dashed lines). The regression lines suggest that medial dendrites branch more extensively as they extend further from the cell body. The scale bars are as follows: A = 200 μm, B = 100 μm, C = 40 μm. Abbreviations: AP – anterior-posterior.

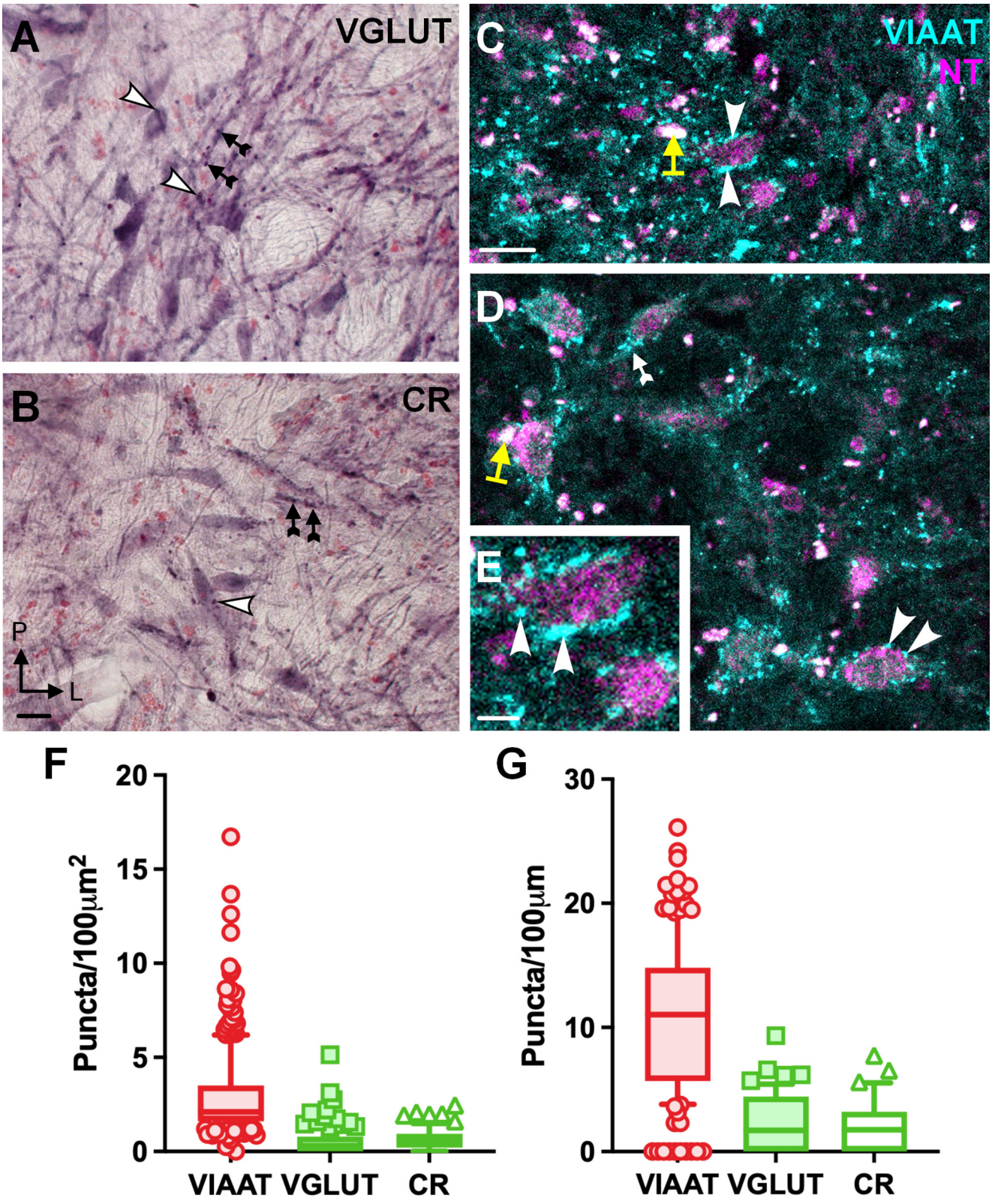

Fig. 3. Distribution of inputs onto MSO soma and proximal dendrites. Immunolabeling for VGLUT is shown in **(A)** and CR immunolabeling is shown in **(B)**. VGLUT and CR+ puncta juxtaposed to cell bodies are indicated by white arrowheads and those in contact with dendrite profiles are indicated by black arrows. Immunolabeling for VIAAT is shown in **(C–E)**. VIAAT+ puncta are densely arranged around MSO cell bodies (white arrowheads) and proximal dendrites (white arrow in **(D)**). The yellow arrows indicate lipofuscin artifact. The scale bar in **(B)** and **(C)** are equal to 20 μm; the scale bar in **(E)** is equal to 10 μm. Figure **(F)** shows the density of puncta associated with cell bodies and **(G)** shows the number of puncta along proximal dendrites. There are noticeably more VIAAT puncta on both MSO somata and proximal dendrites.

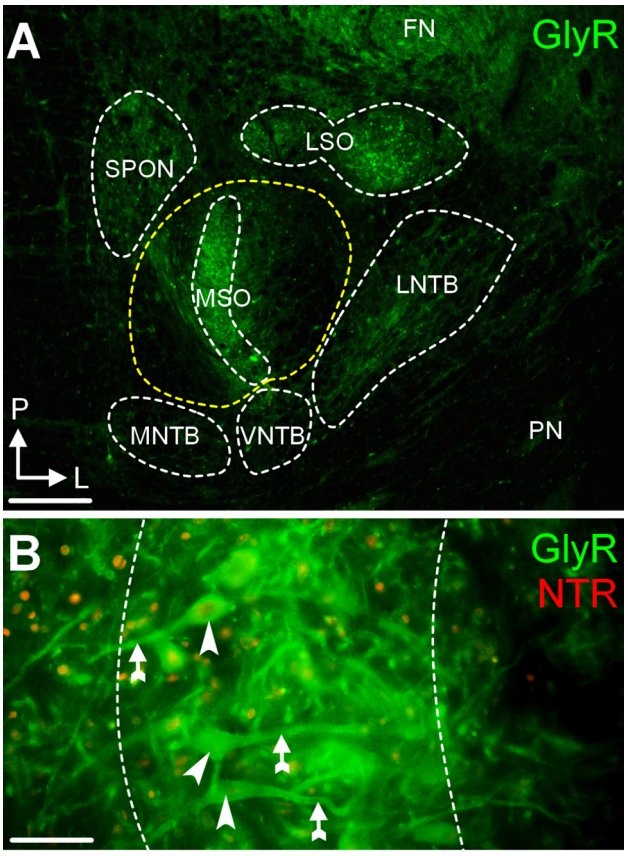

Fig. 4. Distribution of GlyR in the MSO. GlyR immunofluorescence is shown throughout the SOC in **(A)** and within the MSO in **(B)**. There is abundant GlyR labeling in the MSO cell column and much less in the peri-MSO (yellow dashed line), especially near the periphery. In **(B)**, GlyR labeling can been restricted to somata (arrowheads) and dendrites (arrows). The scale bars are as follows: A-500 μm, B-60 μm.

symmetric and have simple branching patterns. This pattern is remarkably similar to what has been reported in cats and gerbils where these medial and lateral dendritic branches are known to segregate inputs from contralateral and ipsilateral ears, respectively (Stotler, 1953; Kiss and Majorossy, 1983; Rautenberg et al., 2009). Further, we provide evidence that inhibitory and excitatory inputs are not uniformly distributed in the human MSO. Specifically, on the cell bodies of human MSO neurons there are four times as many VIAAT+ puncta compared to VGLUT+ or CR+ puncta (Fig. 7). This difference is exacerbated on proximal dendrites where VIAAT+ puncta outnumber VGLUT+/CR+ puncta nearly six to one (Fig. 7). However, on dendrites away from the MSO cell column in the peri-MSO, VIAAT and VGLUT+ puncta are found in nearly equal proportions. In fact, there was no difference in the density of VIAAT+ puncta across the peri-MSO. Although there were more VGLUT+ puncta in the far lateral peri-MSO compared to VIAAT+ puncta. Our reconstructions of MSO neurons suggest that the dendrites occupy approximately nine times more area compared to the soma compartment. As such, MSO dendrites receive and integrate many more inputs than the soma and these dendritic inputs are known to play an important role in sharpening ITD tuning (Golding and Oertel, 2012). However, based on *in vivo* responses from MSO neurons, the glycinergic inputs on the cell body are powerful and have a strong influence on ITD coding (Pecka et al., 2008). Together, our results are consistent with humans utilizing the same ITD circuits described in laboratory animals with excellent low-frequency hearing where inhibitory inputs are also preferentially distributed on MSO cell bodies (Kuwabara and Zook, 1992; Smith et al., 1993; Brand et al., 2002; Kapfer et al., 2002; Pecka et al., 2008; Couchman et al., 2010). It is important to note that such segregation of inputs is not uniform across mammalian species. Animals with hearing ranges centered on higher frequencies do not depend as heavily on ITDs (rats, opossum) and do not show such preferential distribution of glycinergic inputs (Kapfer et al., 2002).

Our findings are consistent with studies of the MSO in non-human primates. In neonatal baboons, MSO cell bodies are associated with dense VGAT/VIAAT labeling whereas VGLUT labeling is concentrated on dendrites (Kim et al., 2014). In the macaque, neurons in the VCN express both VGLUT1 and VGLUT2 while virtually no

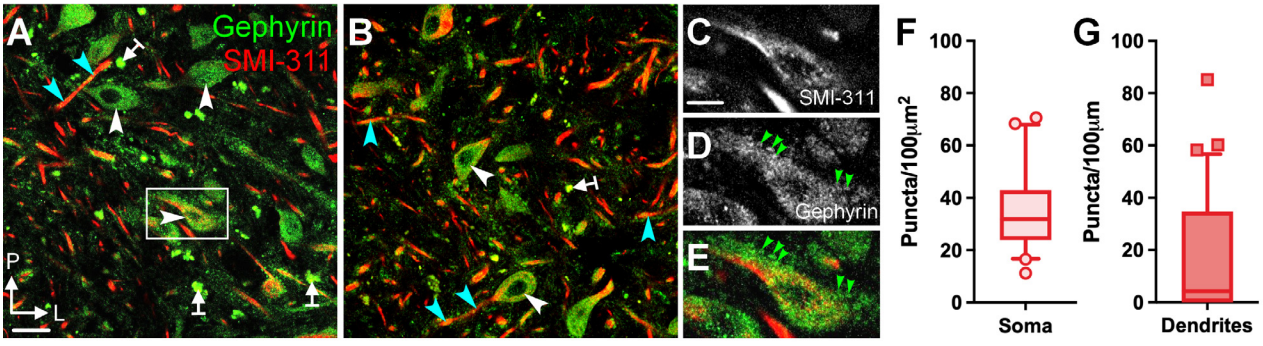

Fig. 5. Distribution of gephyrin in the human MSO. Shown in **(A)** and **(B)** are confocal images showing immunofluorescence for the glycine receptor linker protein gephyrin. Immunolabeling for the neurofilament marker SMI-311 identifies dendritic profiles. Gephyrin+ puncta are heavily distributed over MSO cell bodies (white arrowheads) but are less frequent over dendrites (cyan arrowheads). The white arrows indicate lipofuscin artifact. The scale bar in A is equal to 25 μm. The area of the white box in A is shown enlarged in **(C–E)**. Gephyrin+ puncta are indicated by green arrowheads in **(D)** and **(E)**. The scale bar in **(C–E)** is equal to 10 μm. Figures **(F)** and **(G)** show the density of gephyrin+ puncta over somata and dendrites, respectively.

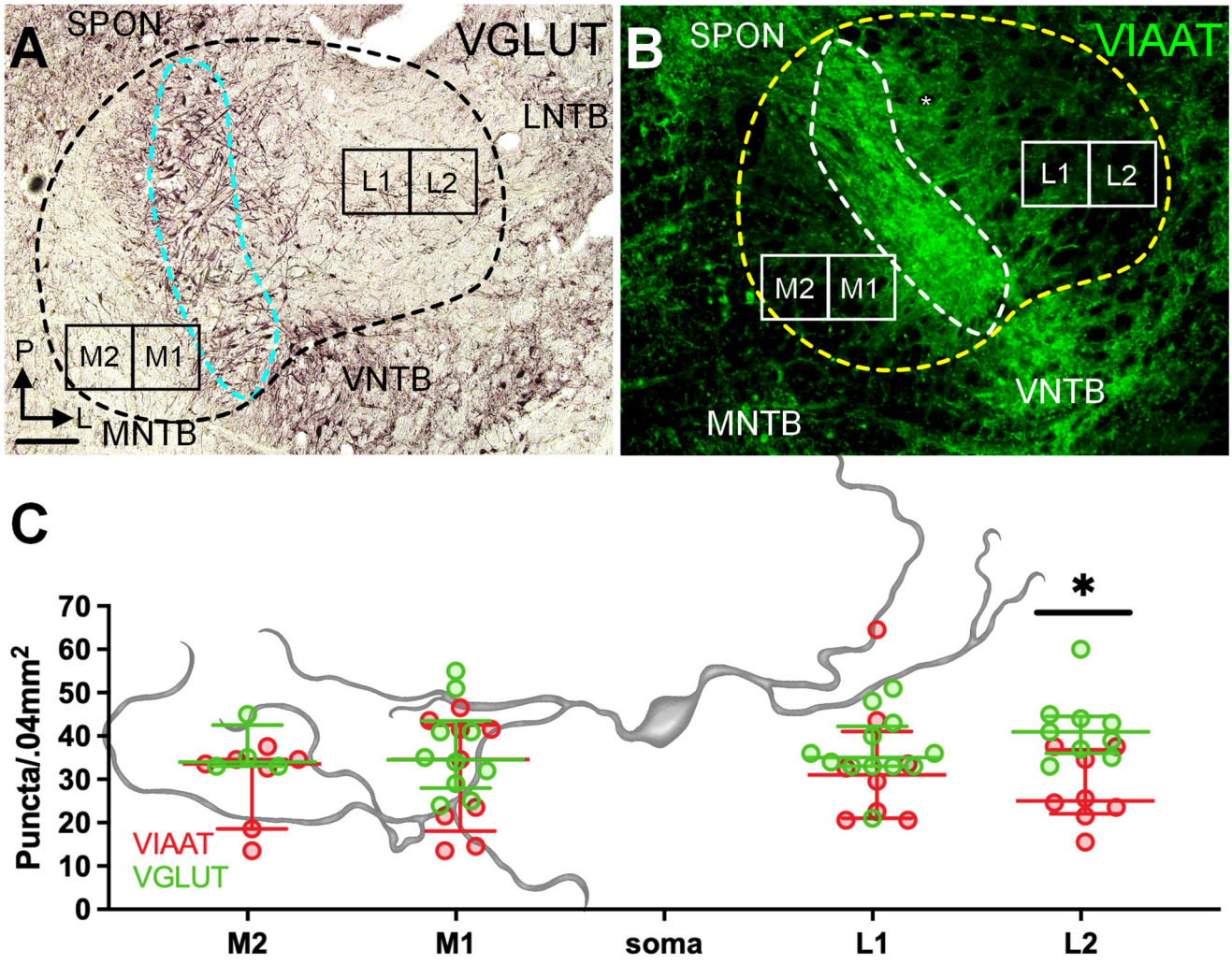

Fig. 6. Distribution of VGLUT and VIAAT in the peri-MSO. Figures **(A)** and **(B)** show VGLUT and VIAAT labeling in the human MSO, respectively. The boxes in the peri-MSO demonstrate representative frames for counting of immunolabeled puncta. The scale bar in A is equal to 200 μm. Figure **(C)** shows the density of VLUT and VIAAT puncta across regions of the medial and lateral peri-MSO. The horizontal lines represent the mean and each circle represents data from one counting frame. VGLUT and VIAAT puncta are uniformly distributed across the peri-MSO fields except for there being significantly more VGLUT puncta in the far lateral field (L2). Key to symbols: * = $p < 0.05$.

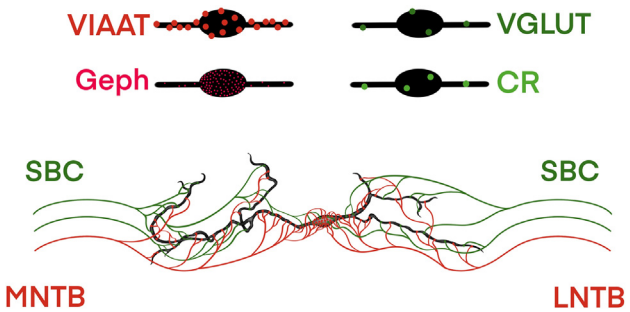

Fig. 7. Summary of inputs to the human MSO. The relative densities of VIAAT, gephyrin, VGLUT, and CR puncta are shown schematically on human MSO cell bodies and proximal dendrites (top). The relative densities and distribution of glutamatergic and glycinergic inputs are shown on a reconstructed human MSO neuron. Green axons indicate glutamatergic inputs from SBCs and red axons indicate glycinergic inputs from the MNTB and LNTB.

neurons in the SOC, nuclei of the lateral lemniscus or inferior colliculus express VGLUT1 (Ito et al., 2015). This provides further evidence that VGLUT terminals we counted in the human MSO are from VCN inputs. Further, neurons in the macaque MNTB express the glycine transporter (GLYT2) consistent with these neurons using glycine as a neurotransmitter (Ito et al., 2015). Additionally, VGLUT1 + puncta were found associated with MSO cell bodies in the macaque, but only few GABAergic terminals were found (Ito et al., 2015). Despite these consistencies with animal models and non-human primates, it is possible we did not label every glutamatergic or glycinergic input and that at least some of the VIAAT puncta were in fact associated with a GABAergic input (see below). Nonetheless, we interpret our findings to indicate that excitatory and inhibitory inputs are segregated on human MSO neurons. Specifically, inhibitory inputs are preferentially distributed on the soma and proximal dendrites while

excitatory inputs are significantly less abundant but more uniformly distributed over the cell body and dendrites.

In addition to glutamatergic and glycinergic inputs, MSO neurons also receive GABAergic inputs from the ipsilateral SPON (Stange et al., 2013). This GABAergic input appears to act primarily at presynaptic $GABA_B$ receptors and functions in adaption and normalization of MSO responses (Stange et al., 2013). While GABAergic inputs to MSO neurons appear less dense than glycinergic inputs (Kulesza and Berrebi, 2000; Couchman et al., 2012; Ito et al., 2015), GABA receptors are present throughout the MSO (Couchman et al., 2012) and are associated with both glutamatergic and glycinergic synapses (Stange et al., 2013). VIAAT, also known as the vesicular GABA transporter (VGAT), transports both GABA and glycine and is found in conjunction with vesicles containing either or both inhibitory neurotransmitters (Dumoulin et al., 1999). Accordingly, we cannot rule out the possibility that some of the VIAAT+ puncta we counted were not associated with a glycinergic terminal. Furthermore, gephyrin anchors glycine receptors including the β subunit and a proportion of $GABA_A$ receptors (Kirsch et al., 1991; Prior et al., 1992). Similarly, we cannot rule out the possibility that some of the gephyrin+ puncta observed in the human MSO are associated with $GABA_A$ receptors and not glycine receptors. Regardless, we do not believe these limitations detract from our conclusion of segregation of excitatory and inhibitory inputs to human MSO neurons. Despite the established roles of GABA in the auditory brainstem, there have been no studies of GABA receptors or GABAergic neurons and terminals in the human SOC.

We have previously described the distribution of CR+ cell bodies, axons and terminals throughout the human auditory brainstem (Kulesza, 2014). We revealed that the vast majority of SBCs in the human VCN are CR+. However, we also found small populations of CR+ neurons in the MNTB (13%), LNTB (11%) and SPON (2%). Our current results indicate no significant differences between the number of VGLUT and CR+ puncta associated with MSO neurons. We interpret this observation to indicate the vast majority of CR+ inputs to the MSO are from SBCs and that only a small percentage of CR+ puncta are from periolivary nuclei.

The human VCN contains approximately 72,000 neurons but the number of SBCs or GBCs is not known (Wagoner and Kulesza, 2009). The human MSO contains about 15,000 neurons (Kulesza, 2007; Kulesza et al., 2011; Lukose et al., 2015), the human MNTB about 3600 neurons and the LNTB about 7500 neurons (Kulesza, 2008; Lukose et al., 2015). Principal neurons in the MNTB are calbindin+ (CB), and in humans approximately 66% of MNTB neurons are CB+ (Kulesza, 2014). The majority of human MNTB neurons are also Kv3.1b+, associated with CR+ calyx terminals and VGLUT and Rab3a+ puncta, consistent with MNTB principal neurons across mammals (Kulesza, 2014). If we consider the CB+ MNTB neurons as providing glycinergic input from the contralateral ear to the MSO, this will equate to about 2400 neurons, or about 6 MSO neurons per projecting MNTB neuron.

While the MNTB is a rather homogenous population of neurons, the LNTB includes a number of different subregions based on location, inputs and neurochemistry (Spirou and Berrebi, 1996). In animal models, neurons in the posteroventral LNTB (pvLNTB) are glycinergic, receive large calyx terminals from GBCs and project to the ipsilateral MSO (Tolbert et al., 1982; Adams, 1983; Grothe and Sanes, 1993; Spirou et al., 1990, 1998; Smith et al., 1991; Cant and Hyson, 1992; Kuwabara and Zook, 1992; Spirou and Berrebi, 1996, 1997; Franken et al., 2016). While we have previously examined neuronal morphology in the human LNTB, designation into subregions or correlations of cell body morphology was not attempted (Kulesza, 2008). Although, about 33% of human LNTB neurons are CB+ and 24% of LNTB somata are associated with large calyx-like CR+ terminals (Kulesza, 2014). Similar to the human MNTB, we interpret these CR+ inputs to be derived from GBCs (Kulesza, 2014). If we consider the CB+ LNTB neurons with CR+ terminals as sources of glycinergic input to the lateral MSO, this would equal ~6 MSO neurons per projecting LNTB neuron, nearly matching the projection to the medial MSO from the MNTB. Interestingly, the cat LNTB includes approximately 9000 neurons with only about 1600 in the pvLNTB (Spirou and Berrebi, 1996), but the cat MSO includes only about 4600 neurons (Fech et al., 2017). We interpret this observation to suggest that while the same basic ITD circuit is used across animals, certain proportions and parameters are species specific. Furthermore, little is known about the role the LNTB plays in the human auditory pathway. The human LNTB is composed of a heterogenous population of neuron morphologies (Kulesza, 2008) and occupies more than twice the brain volume as the MSO (Mansour and Kulesza, 2020) and it is not clear how the structure of the human LNTB correlates with subregions designated in cat and gerbil (Spirou and Berrebi, 1997; Spirou et al., 1998; Franken et al., 2016). Finally, like the glutamatergic inputs from the SBC to the MSO, the inputs to/from the LNTB and MNTB must account for different axon lengths from each ear and these differences are exacerbated in humans because of head and brain size. Additionally, there is evidence that GBC axonal diameter, myelination and internodal lengths vary according to best-frequency in gerbils (Ford et al., 2015). How the human ITD circuit is modified to account for these specific issues is unknown.

Our results indicate that human MSO neurons form simple and symmetric dendritic arbors similar to those in low-frequency hearing animals utilizing ITDs. Additionally, we provide evidence that inhibitory inputs associated with VIAAT are predominantly located along cell bodies and proximal dendrites of MSO neurons. This is supported by localization of glycine receptors on MSO somata and heavy distribution of the glycine and GABA receptor anchoring protein gephyrin. Our results also suggest that glutamatergic inputs from the VCN associated with VGLUT are comparatively sparse but are distributed along the entire MSO neuron. These results are consistent with characterization of the ITD

circuit in gerbils and suggest that humans use the same basic plan.

ACKNOWLEDGEMENTS

The authors are grateful to the families of the donors, who have made this study possible.

AUTHOR CONTRIBUTIONS

Yusra Mansour – designed the study, conducted experiments, collected data, constructed figures, reviewed and edited the manuscript; Randy Kulesza – designed and oversaw the study, provided resources, analyzed data, wrote the original draft, reviewed and edited the manuscript.

FUNDING SOURCES

This research was funded by a grant from the Lake Erie Consortium for Osteopathic Medical Training.

REFERENCES

Adams JC (1981) Heavy metal intensification of DAB-based HRP reaction product. J Histochem Cytochem 29(6):775.
Adams JC (1983) Cytology of periolivary cells and the organization of their projections in the cat. J Comp Neurol 215(3):275–289.
Aparicio M-A, Saldaña E (2014) The dorsal tectal longitudinal column (TLCd): a second longitudinal column in the paramedian region of the midbrain tectum. Brain Struct Funct 219(2):607–630.
Banks MI, Smith PH (1992) Intracellular recordings from neurobiotin labeled cells in brain slices of the rat medial nucleus of the trapezoid body. J Neurosci 12(7):2819–2837.
Bazwinsky I, Hilbig H, Bidmon HJ, Rubsamen R (2003) Characterization of the human superior olivary complex by calcium binding proteins and neurofilament (SMI-32). J Comp Neurol 456:292–303.
Brand A, Behrend O, Marquardt T, McAlpine D, Grothe B (2002) Precise inhibition is essential for microsecond interaural time difference coding. Nature 417(6888):543–547.
Cant NB, Hyson RL (1992) Projections from the lateral nucleus of the trapezoid body to the medial superior olivary nucleus in the gerbil. Hear Res 58(1):26–34.
Clark GM (1969) Vesicle shape versus type of synapse in the nerve endings of the cat medial superior olive. Brain Res 15 (2):548–551.
Couchman K, Grothe B, Felmy F (2010) Medial superior olivary neurons receive surprisingly few excitatory and inhibitory inputs with balanced strength and short-term dynamics. J Neurosci 30 (50):17111–17121.
Couchman K, Grothe B, Felmy F (2012) (2012) Functional localization of neurotransmitter receptors and synaptic inputs to mature neurons of the medial superior olive. J Neurophysiol. 107 (4):1186–1198.
Dumoulin A, Rostaing P, Bedet C, Lévi S, Isambert MF, Henry JP, Triller A, Gasnier B (1999) Presence of the vesicular inhibitory amino acid transporter in GABAergic and glycinergic synaptic terminal boutons. J Cell Sci 112(Pt 6):811–823.
Fech T, Calderón-Garcidueñas L, Kulesza Jr RJ (2017) Characterization of the superior olivary complex of Canis lupus domesticus. Hear Res 351:130–140.
Feng AS, Rogowski BA (1980) Effects of monaural and binaural occlusion on the morphology of neurons in the medial superior olivary nucleus of the rat. Brain Res 189(2):530–534.
Ford MC, Alexandrova O, Cossell L, Stange-Marten A, Sinclair J, Kopp-Scheinpflug C, Pecka M, Attwell D, Grothe B (2015) Tuning of Ranvier node and internode properties in myelinated axons to adjust action potential timing. Nat Commun 6:8073.
Franken TP, Smith PH, Joris PX (2016) In vivo whole-cell recordings combined with electron microscopy reveal unexpected morphological and physiological properties in the lateral nucleus of the trapezoid body in the auditory brainstem. Front Neural Circuits 10:69.
Friauf E, Ostwald J (1988) Divergent projections of physiologically characterized rat ventral cochlear nucleus neurons as shown by intra-axonal injection of horseradish peroxidase. Exp Brain Res 73(2):263–284.
Friedland DR, Los JG, Ryugo DK (2006) A modified Golgi staining protocol for use in the human brain stem and cerebellum. J Neurosci Methods 150(1):90–95.
Goldberg JM, Brown PB (1969) Response of binaural neurons of dog superior olivary complex to dichotic tonal stimuli: some physiological mechanisms of sound localization. J. Neurophysiol 32(4):613–636.
Golding NL, Oertel D (2012) Synaptic integration in dendrites: exceptional need for speed. J Physiol 590(22):5563–5569.
Grothe B, Sanes DH (1993) Bilateral inhibition by glycinergic afferents in the medial superior olive. J Neurophysiol 69 (4):1192–1196.
Grothe B, Pecka M, McAlpine D (2010) Mechamisms of sound localization in mammals. Physiol Rev 90:983–1012.
Guinan JJ, Norris BE, Guinan SS (1972) Single auditory units in the superior olivary complex II: locations of unit categories and tonotopic organization. Int J Neurosci 4 (4):147–166.
Hilbig H, Beil B, Hilbig H, Call J, Bidmon H-J (2009) Superior olivary complex organization and cytoarchitecture may be correlated with function and catarrhine primate phylogeny. Brain Struct Funct 213 (4-5):489–497.
Iñiguez C, Gayoso MJ, Carreres J (1985) A versatile and simple method for staining nervous tissue using Giemsa dye. J Neurosci Methods 13(1):77–86.
Ito T, Inoue K, Takada M (2015) Distribution of glutamatergic, GABAergic, and glycinergic neurons in the auditory pathways of macaque monkeys. Neuroscience 310:128–151.
Jeffress LA (1948) A place theory of sound localization. J Comp Physiol Psychol 41(1):35–39.
Kapfer C, Seidl AH, Schweizer H, Grothe B (2002) Experience-dependent refinement of inhibitory inputs to auditory coincidence-detector neurons. Nat Neurosci 5(3):247–253.
Kim SE, Lee SY, Blanco CL, Kim JH (2014) Developmental profiles of the intrinsic properties and synaptic function of auditory neurons in preterm and term baboon neonates. J Neurosci 34 (34):11399–11404.
Kirsch J, Langosch D, Prior P, Littauer UZ, Schmitt B, Betz H (1991) The 93-kDa glycine receptor-associated protein binds to tubulin. J Biol Chem 266(33):22242–22245.
Kiss A, Majorossy K (1983) Neuron morphology and synaptic architecture in the medial superior olivary nucleus. Light- and electron microscope studies in the cat. Exp Brain Res 52 (3):315–327.
Klumpp RG, Eady HR (1956) Some measurements of interaural time difference thresholds. J Acoust Soc Am 28(5):859–860.
Kulesza Jr RJ (2014) Characterization of human auditory brainstem circuits by calcium-binding protein immunohistochemistry. Neuroscience 258:318–331.
Kulesza Jr RJ, Berrebi AS (2000) Superior paraolivary nucleus of the rat is a GABAergic nucleus. J Assoc Res Otolaryngol 1 (4):255–269.
Kulesza Jr RJ, Grothe B (2015) Yes, there is a medial nucleus of the trapezoid body in humans. Front Neuroanat 9:35.
Kulesza Jr RJ, Lukose R, Stevens LV (2011) Malformation of the human superior olive in autistic spectrum disorders. Brain Res 1367:360–371.
Kulesza Jr RJ (2007) Cytoarchitecture of the human superior olivary complex: medial and lateral superior olive. Hear Res 225(1–2):80–90.

Kulesza Jr RJ (2008) Cytoarchitecture of the human superior olivary complex: nuclei of the trapezoid body and posterior tier. Hear Res 241(1–2):52–63.
Kuwabara N, DiCaprio RA, Zook JM (1991) Afferents to the medial nucleus of the trapezoid body and their collateral projections. J Comp Neurol 314(4):684–706.
Kuwabara N, Zook JM (1992) Projections to the medial superior olive from the medial and lateral nuclei of the trapezoid body in rodents and bats. J Comp Neurol. 324(4):522–538.
Lukose R, Beebe K, Kulesza Jr RJ (2015) Organization of the human superior olivary complex in 15q duplication syndromes and autism spectrum disorders. Neuroscience 286:216–230.
Mansour Y, Kulesza R (2020) Three dimensional reconstructions of the superior olivary complex from children with autism spectrum disorder. Hear Res 393:107974.
Márquez-Legorreta E, Horta-Júnior Jde A, Berrebi AS, Saldaña E (2016) Organization of the zone of transition between the pretectum and the thalamus, with emphasis on the pretectothalamic lamina. Front Neuroanat 10:82.
Moore JK (1987) The human auditory brainstem: a comparative view. Hear Res 29(1):1–32.
Moore JK, Moore RY (1971) Comparative study of the superior olivary complex in the primate brain. Folia Primatol (Basel) 16:35–51.
Morest DK (1968a) The collateral system of the medial nucleus of the trapezoid body of the cat, its neuronal architecture and relation to the olivo-cochlear bundle. Brain Res 9(2):288–311.
Morest DK (1968b) The growth of synaptic endings in the mammalian brain: a study of the calyces of the trapezoid body. Z Anat Entw Gesch 127(3):201–220.
Myoga MH, Lehnert S, Leibold C, Felmy F, Grothe B (2014) Glycinergic inhibition tunes coincidence detection in the auditory brainstem. Nat Commun 5:3790.
Pecka M, Brand A, Behrend O, Grothe B (2008) Interaural time difference processing in the mammalian medial superior olive: the role of glycinergic inhibition. J Neurosci 28(27):6914–6925.
Prior P, Schmitt B, Grenningloh G, Pribilla I, Multhaup G, Beyreuther K, Maulet Y, Werner P, Langosch D, Kirsch J, Betz H (1992) Primary structure and alternative splice variants of gephyrin, a putative glycine receptor-tubulin linker protein. Neuron 8 (6):1161–1170.
Rautenberg PL, Grothe B, Felmy F (2009) Quantification of the three-dimensional morphology of coincidence detector neurons in the medial superior olive of gerbils during late postnatal development. J Comp Neurol 517(3):385–396.
Roberts MT, Seeman SC, Golding NL (2014) The relative contributions of MNTB and LNTB neurons to inhibition in the medial superior olive assessed through single and paired recordings. Front Neural Circuits 8:49.
Schneider CA, Rasband WS, Eliceiri KW (2012) NIH Image to ImageJ: 25 years of image analysis. Nat Methods 9(7):671–675.
Smith PH (1995) Structural and functional differences distinguish principal from nonprincipal cells in the guinea pig MSO slice. J Neurophysiol 73(4):1653–1667.
Smith PH, Joris PX, Yin TC (1993) Projections of physiologically characterized spherical bushy cell axons from the cochlear nucleus of the cat: evidence for delay lines to the medial superior olive. J Comp Neurol 331(2):245–260.
Smith PH, Joris PX, Yin TC (1998) Anatomy and physiology of principal cells of the medial nucleus of the trapezoid body (MNTB) of the cat. J Neurophysiol 79(6):3127–3142.
Smith PH, Joris PX, Carney LH, Yin TCT (1991) Projections of physiologically characterized globular bushy cell axons from the cochlear nucleus of the cat. J Comp Neurol 304 (3):387–407.
Spirou GA, Berrebi AS (1996) Organization of ventrolateral periolivary cells of the cat superior olive as revealed by PEP-19 immunocytochemistry and Nissl stain. J Comp Neurol 368 (1):100–120.
Spirou GA, Berrebi AS (1997) Glycine immunoreactivity in the lateral nucleus of the trapezoid body of the cat. J Comp Neurol 383 (4):473–488.
Spirou GA, Brownell WE, Zidanic M (1990) Recordings from cat trapezoid body and HRP labeling of globular bushy cell axons. J Neurophysiol 63(5):1169–1190.
Spirou GA, Rowland KC, Berrebi AS (1998) Ultrastructure of neurons and large synaptic terminals in the lateral nucleus of the trapezoid body of the cat. J Comp Neurol 398(2):257–272.
Spitzer MW, Semple MN (1995) Neurons sensitive to interaural phase disparity in gerbil superior olive: diverse monaural and temporal response properties. J Neurophysiol 73 (4):1668–1690.
Stange A, Myoga MH, Lingner A, Ford MC, Alexandrova O, Felmy F, Pecka M, Siveke I, Grothe B (2013) Adaptation in sound localization: from GABA(B) receptor-mediated synaptic modulation to perception. Nat Neurosci 16(12):1840–1847.
Stotler WA (1953) An experimental study of the cells and connections of the superior olivary complex of the cat. J Comp Neurol 98 (3):401–431.
Strominger NL, Hurwitz JL (1976) Anatomical aspects of the superior olivary complex. J Comp Neurol 170:485–497.
Taschenberger H, Leão RM, Rowland KC, Spirou GA, von Gersdorff H (19) (2002) Optimizing synaptic architecture and efficiency for high-frequency transmission. Neuron 36(6):1127–1143.
Tolbert LP, Morest DK, Yurgelun-Todd DA (1982) The neuronal architecture of the anteroventral cochlear nucleus of the cat in the region of the cochlear nerve root: horseradish peroxidase labelling of identified cell types. Neuroscience 7 (12):3031–3052.
van der Heijden M, Lorteije JA, Plauška A, Roberts MT, Golding NL, Borst JG (2013) Directional hearing by linear summation of binaural inputs at the medial superior olive. Neuron 78 (5):936–948.
Wagoner JL, Kulesza Jr RJ (2009) Topographical and cellular distribution of perineuronal nets in the human cochlear nucleus. Hear Res 254(1–2):42–53.
Yin TC, Chan JC (1990) Interaural time sensitivity in medial superior olive of cat. J Neurophysiol 64(2):465–488.

(Received 3 January 2021, Accepted 3 June 2021)
(Available online 12 June 2021)